Solution Conformation of the (+)-*trans-anti*-[BPh]dA Adduct opposite dT in a DNA Duplex: Intercalation of the Covalently Attached Benzo[*c*]phenanthrene to the 5′-Side of the Adduct Site without Disruption of the Modified Base Pair†

Monique Cosman,‡ Radovan Fiala,‡ Brian E. Hingerty,§ Alfred Laryea,∥ Hongmee Lee,⊥ Ronald G. Harvey,⊥ Shantu Amin,▽ Nicholas E. Geacintov,∥ Suse Broyde,∞ and Dinshaw Patel*,‡

Cellular Biochemistry and Biophysics Program, Memorial Sloan-Kettering Cancer Center, 1275 York Avenue, New York, New York 10021, Health and Safety Research Division, Oak Ridge National Laboratory, Oak Ridge, Tennessee 37831, Chemistry and Biology Departments, New York University, New York, New York 10003, Ben May Institute, University of Chicago, Chicago, Illinois 60637, and American Health Foundation, Dana Road, Valhalla, New York 10595

Received July 30, 1993; Revised Manuscript Received September 17, 1993•

ABSTRACT: Benzo[*c*]phenanthrene diol epoxide can covalently bind to the exocyclic amino group of deoxyadenosine to generate [BPh]dA adducts where the polycyclic aromatic hydrocarbon is attached to the major groove edge of DNA. This paper reports on NMR–energy minimization structural studies of the (+)-*trans-anti*-[BPh]dA adduct positioned opposite dT in the sequence context d(C5-[BPh]A6-C7)·d-(G16-T17-G18) at the 11-mer duplex level. The exchangeable and nonexchangeable protons of the benzo-[*c*]phenanthrenyl moiety and the nucleic acid were assigned following analysis of two-dimensional NMR data sets in H_2O and D_2O solution. The solution structure of the (+)-*trans-anti*-[BPh]dA·dT 11-mer duplex has been determined by incorporating intramolecular and intermolecular proton–proton distances defined by upper and lower bounds deduced from NOESY data sets as restraints in energy minimization computations. The covalently attached benzo[*c*]phenanthrene ring intercalates to the 5′-side of the [BPh]-dA6 lesion site without disruption of the flanking Watson–Crick dC5·dG18 and [BPh]dA6·dT17 base pairs. The observed buckling of the intercalation cavity reflects the selective overlap of the intercalated phenanthrenyl ring with dT17 and dG18 bases on the unmodified strand. The structure provides new insights into how a polycyclic aromatic hydrocarbon covalently attached to the major groove edge of deoxyadenosine can still unidirectionally intercalate into the helix without disruption of the modified base pair. Our study establishes that among the contributing factors are a propeller-twisted [BPh]dA6·dT17 base pair, displacement of the carcinogen–DNA linkage bond from the plane of the dA6 base, the specific pucker adopted by the benzylic ring, and the propeller-like nonplanar geometry for the aromatic phenanthrenyl ring system. Our combined experimental–computational studies to date have now identified three structural motifs adopted by covalent polycyclic aromatic hydrocarbon–DNA adducts with their distribution determined by the chiral characteristics of individual stereoisomers and by whether the covalent adducts are generated at the minor or the major groove edge of the helix.

Polycyclic aromatic hydrocarbons (PAH) are an important class of environmental pollutants (Lunde & Bjorseth, 1977), which in themselves are chemically inert until they are metabolically activated in living cells to highly reactive bay region diol epoxides [reviewed in Miller (1978), Conney (1982), and Singer and Grunberger (1983)]. Benzo[*c*]-phenanthrene (B[*c*]Ph) is a weakly tumorigenic PAH that is metabolized in cellular systems to a small extent to bay region 1,2,3,4-tetrahydro-3,4-diol 1,2-epoxides (B[*c*]PhDE) (1) (Chart 1) (Jerina et al., 1984; Thakker et al., 1986; Pruess-Schwartz et al., 1984). These B[*c*]Ph diol epoxides occur as a pair of diastereomers in which the hydroxyl group at the 4-position can be either *syn* (diol epoxide 1) or *anti* (diol epoxide 2) to the oxirane oxygen (Yagi et al., 1983). Furthermore, each of these is composed of a (+) and a (–) optical enantiomer. Unlike benzo[*a*]pyrene diol epoxides (B[*a*]PDE) which react predominantly with deoxyguanosine (Cheng et al., 1989), the B[*c*]PhDEs react extensively with both deoxyguanosine and deoxyadenosine *in vitro* (Dipple et al., 1987; Agarwal et al., 1987; Canella et al., 1992) and in rodent embryo cell cultures (Pruess-Schwartz et al., 1987). Sixteen principal adducts have been identified *in vitro* (Agarwal et al., 1987; Canella et al., 1992).

The mutagenic and tumorigenic activities of the (+)- and (–)-*anti*-B[*c*]PhDE optical enantiomers have been extensively studied. Both are tumorigenic (Levin et al., 1986) and mutagenic (Wood et al., 1984; Bigger et al., 1989, 1992). Bigger et al. (1989, 1992) used a pS189 shuttle vector carrying a *supF* gene modified by each B[*c*]Ph diol epoxide isomer to study the mutational spectrum obtained in replicating human cells. Mutations were targeted to both dA and dG for both isomers as expected for adducts at the two sites, and the most frequent point mutation observed was a deoxypurine to dT transversion.

† This research was supported by NIH Grants CA-46533 and CA-21111 to D.J.P.; by NIH Grant CA-20851 and U.S. DOE Grant DE-FG02-88ER60405 to N.E.G.; by NIH Grant CA-28038, NIH Grant RR-06458, and U.S. DOE Grant DE-FG02-90ER60931 to S.B.; by U.S. DOE Contract DE-AC05-840R21400 with Martin Marietta Energy Systems, Inc., and U.S. DOE OHER Field Work Proposal ERKP931 to B.E.H.; and by NIH Grant ES-04732 and American Cancer Society Grant CN-22 to R.H.

‡ Memorial Sloan-Kettering Cancer Center.
§ Oak Ridge National Laboratory.
∥ Chemistry Department, New York University.
⊥ University of Chicago.
▽ American Health Foundation.
∞ Biology Department, New York University.

• Abstract published in *Advance ACS Abstracts*, November 1, 1993.

0006-2960/93/0432-12488$04.00/0

Chart I

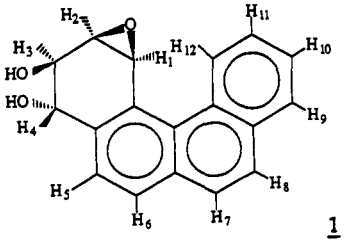

1

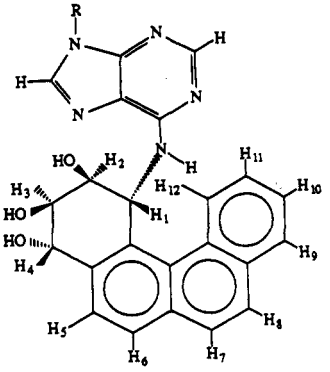

2

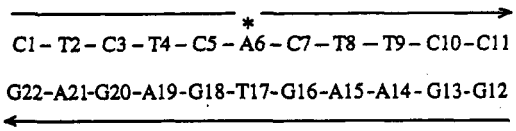

3

We have recently reported on the solution structures of three stereoisomeric benzo[*a*]pyrene diol epoxide [BP]dG adducts positioned opposite dC in the d(C-[BP]G-C)·d(G-C-G) sequence context at the duplex level (Cosman et al., 1992, 1993; de los Santos et al., 1992). These studies established that either the covalent [BP]dG adducts were positioned in the minor groove without perturbation of the modified base pair [(+)- and (−)-*trans-anti* stereoisomers] or the benzo[*a*]pyrene intercalated into the helix with disruption of the modified base pair [(+)-*cis-anti* stereoisomer]. In the present paper we have applied two-dimensional NMR techniques in combination with energy minimization computations to elucidate the solution structure of the (+)-*trans-anti*-[BPh]-dA adduct **2** positioned opposite dT in the d(C-[BPh]A-C)·d-(G-T-G) sequence context of duplex **3** [designated (+)-*trans-anti*-[BPh]dA·dT 11-mer duplex]. Our results demonstrate that the covalently attached benzo[*c*]phenanthrene ring intercalates to the 5′-side of the [BPh]dA adduct site without disruption of the [BPh]dA·dT base pair.

MATERIALS AND METHODS

Preparation of (+)-trans-anti-[BPh]dA·dT 11-mer Duplex. Racemic *anti*-B[*c*]PhDE was synthesized according to published procedures (Misra & Amin, 1990). A 7 mM stock solution of *anti*-B[*c*]PhDE in THF was prepared and used in the modification of oligonucleotides. The modified oligonucleotide d(C-T-C-T-C-[BPh]A-C-T-T-C-C), in which the exocyclic amino group of deoxyadenosine is modified covalently by *trans* addition of (+)-*anti*-B[*c*]PhDE, was prepared by a direct synthesis procedure along the lines described by Cosman et al. (1990) for B[*a*]PDE. Only a brief summary of the method is provided here, since a paper describing the details of the synthesis and the characterization of the adducts is in preparation (A. Laryea, V. Ibanez, M. Cosman, S. Amin, R. G. Harvey, and N. E. Geacintov, in preparation).

The oligonucleotide d(C-T-C-T-C-A-C-T-T-C-C) was synthesized by the phosphoramidite method and purified as described earlier (Cosman et al., 1990). A 0.5 mM (strand concentration) solution of the oligonucleotide was prepared in 50 mM sodium acetate, pH 5.0. A reaction mixture consisting of 3 mL of the epoxide–THF solution and 10 mL of the aqueous oligonucleotide solution was prepared, and an additional 1.5 mL of THF was added in order to prevent the partial precipitation of *anti*-B[*c*]PhDE (molar ratio B[*c*]PhDE: strand = 4:1). This solution was incubated at room temperature for 4 days. The completion of the reaction was verified by the absence of *anti*-B[*c*]PhDE in the reaction mixture (determined by reverse-phase HPLC using a Hitachi Intelligent Pump L-6200A, Hitachi Instruments, Inc., Danbury, CT). The THF was evaporated using a flash evaporator (Buchler Instruments, Fort Lee, NJ). As a result of the removal of the organic solvent, a fraction of the hydrolysis products of *anti*-B[*c*]PhDE (mostly tetraols) precipitated, and these were removed by centrifugation. The oligonucleotide adducts were separated from the unmodified oligonucleotides using reverse-phase HPLC methods. The column used was a 5-μm Hypersil ODS 250 × 10 mm column with a pore size of 120 Å (Keystone Scientific, Inc., Bellefonte, PA). The elution gradient was 0–90% methanol/20 mM sodium phosphate buffer (pH 7.0) for 60 min. The unmodified oligonucleotide appeared typically within the 20–23-min interval, while the *anti*-B[*c*]PhDE modified oligonucleotides appeared between 25 and 26 min (the adducts were characterized by two overlapping and poorly resolved peaks). The unmodified and modified oligonucleotides (typical overall yields were 10 ± 2%, based on the amount of oligonucleotides present initially) were collected separately. The adducts were separated by a second HPLC gradient (20–24% methanol/phosphate buffer gradient for 120 min). The elution profile exhibited two major broad peaks eluting at 35–45 and 65–75 min, respectively (the ratio of the areas of the first and second peaks was ~2:1), and each of these fractions was collected separately. The first fraction contained the (+)-*trans-anti*-B[*c*]PhDE–N^6-dA-modified oligonucleotide, while the second fraction contained the (-)-*trans-anti*-B[*c*]PhDE–N^6-dA-modified oligonucleotide (see below). The first eluate used in these experiments was further purified by reverse-phase HPLC using time and gradient intervals (0–20% methanol/phosphate buffer for 10 min, followed by 20–40% methanol/phosphate buffer for 60 min); a single major eluate peak was observed, and this fraction was collected. The solution was desalted using a G-25 Sephadex column and evaporated to dryness. This procedure was repeated five times in order to accumulate sufficient material (a total of 130 OD units of modified oligonucleotides) for the NMR experiments.

In order to establish the identity of the *anti*-B[*c*]PhDE oligonucleotide adduct, the first HPLC elution fraction was digested with spleen exonuclease (phosphodiesterase II, Worthington Biochemical Corporation, Freehold, NJ) as described by Razzel and Khorana (1961). The unmodified deoxyribonucleosides were separated from the B[*c*]PhDE-modified deoxyadenosine using reverse-phase HPLC (0–90% methanol/20 mM phosphate buffer, pH 7.0, for 60 min, using the same column as above). The adducted adenosine eluted at 45 min, and its elution time coincided with that of a (+)-*trans-anti*-B[*c*]PhDE–N^6-dA adduct standard, which was prepared by reacting the enantiomer (+)-*anti*-B[*c*]PhDE with dA and characterized according to the methods described by Agarwal et al. (1987) and by Dipple et al. (1987) using CD and UV absorption spectroscopy.

The modified enantiomerically pure d(C-T-C-T-C-[BPh]A-C-T-T-C-C) strand was annealed to its complementary unmodified d(G-G-A-A-G-T-G-A-G-A-G) strand at 70 °C,

and the stoichiometry was followed by monitoring single proton resonances in both strands.

NMR Experiments. A combination of through-space nuclear Overhauser enhancement (NOESY) and through-bond correlated (COSY, HOHAHA) two-dimensional spectra were recorded and analyzed to assign the benzo[*c*]phenanthrene and nucleic acid protons in the (+)-*trans-anti*-[BPh]-dA·dT 11-mer duplex. NOESY data sets on the modified duplex (9 mg) in H_2O buffer (0.6 mL of 0.1 M NaCl, 10 mM phosphate, and 0.1 mM EDTA, pH 7.0) at 1 °C were recorded at mixing times of 60, 100, and 150 ms using a jump and return pulse for solvent suppression. The corresponding data sets on the modified duplex in D_2O buffer at 25 °C were recorded at mixing times of 40, 50, 80, 120, 160, and 300 ms. Through-bond relay connectivities in HOHAHA data sets were recorded at spin-lock times of 40, 80, and 120 ms in D_2O buffer at 25 °C.

Several factors went into the conversion of the NOE intensities into the distance bounds used for the structure determination. The interproton distance calculations were based on the isolated two-spin approximation using the dT(NH3)–dA(H2) fixed distance of 2.92 Å for the NOESY data sets in H_2O and the dC(H6)–dC(H5) fixed distance of 2.45 Å for the NOESY data sets in D_2O solution. The choice of upper- and lower-bound ranges on the estimated distances depended on the resolution of the cross peaks in the contour plots. The base proton to sugar H1′ NOE cross peaks in the shortest mixing time NOESY data set in D_2O were evaluated to qualitatively differentiate between *syn* (strong NOE) and *anti* (weak NOE) glycosidic torsion angles (Patel et al., 1982).

The proton–proton vicinal coupling constant patterns were computed using the SPHINX and LINSHA programs (K. Wuthrich, ETH, Zurich) to constrain torsion angles linking BPh(H1)–BPh(H2) and BPh(H3)–BPh(H4) proton pairs in the benzylic ring of [BPh]dA. We monitored coupling constant patterns to qualitatively distinguish between the different families of nucleic acid sugar puckers in the (+)-*trans-anti*-[BPh]dA·dT 11-mer duplex. The relative intensities of the NOE cross peaks between the base protons and their own and 5′-flanking sugar H2′, H2″, and H3′ protons were also used to qualitatively distinguish between the A and B families of sugar puckers for the adduct duplex (van de Ven & Hilbers, 1988).

Energy Minimization Computations. Minimized potential energy calculations were carried out with DUPLEX, a molecular mechanics program for nucleic acids that performs potential energy minimizations in the reduced-variable domain of torsion angle space (Hingerty et al., 1989). The advantage of torsion space, compared to Cartesion space, minimizations is the vast diminution in the number of variables that must be simultaneously optimized, thereby permitting larger movements from a given starting conformation during minimization, as well as assurance of realistic internal geometry.

DUPLEX uses a potential set similar to the one developed by Olson and co-workers for nucleic acids (Taylor & Olson, 1983), and details have been published previously (Hingerty et al., 1989). Force-field parameters for the (+)-*trans-anti*-[BPh]dA adduct were the same as those employed for the analogous (+)-*trans-anti*-[BP]dG adduct (Hingerty & Broyde, 1985; Singh et al., 1991) except that new partial charges had to be computed for the carcinogen and for the linkage site (Figure S1, supplementary material). This was accomplished for the (+)-*trans-anti*-[BPh]dA adduct with the CNDO module of the program CHEM-X (Chemical Design, Ltd., Mahwah, NJ) which yields partial charges compatible with the set employed in DUPLEX (Ornstein & Rein, 1979). The geometry (bond length, bond angles, and dihedral angles) of the [BPh]dA adduct was generated from that employed for the [BP]dG adducts (Hingerty & Broyde, 1985; Singh et al., 1991) by computer graphics on a Silicon Graphics Personal Iris Model 4D-35 with the program INSIGHT (Biosym Technologies, Inc., Parsippany, NJ). In one geometry, the conformation of the benzylic ring was in the distorted half-chair form with the BPh(H1) and BPh(H2) protons in the diequatorial domain and the BPh(H3) and BPh(H4) protons in the diaxial domain (Neidle et al., 1982). In addition, a second geometry was built with INSIGHT which placed the BPh(H1) and BPh(H2) protons in the diaxial domain and the BPh(H3) and BPh(H4) protons in the diequatorial domain. These two (+)-*trans-anti*-BPh adducts to deoxyadenosine were then energy minimized with MacroModel V3.5X (Mohamadi et al., 1990) using the MacroModel implementation of the MM3 force field (MM3*) with the solvent and extended nonbonded cutoff option. These two MacroModel minimized (+)-*trans-anti*-[BPh]dA structures (supplementary Figure S2) were then implemented within DUPLEX.

A hydrogen bond penalty function (Hingerty et al., 1989) was employed in all first-stage minimizations to aid the minimizer in locating the Watson–Crick hydrogen-bonded structures indicated by the NMR data. To locate minimum energy conformations with interproton distances available from the experimental NMR data, pseudopotentials (permitting upper and lower bound restraints) were added to the energy, as described previously (Norman et al., 1989; Schlick et al., 1990; Cosman et al., 1992, 1993). Briefly, the following functions were used:

$$F_N = W_N \sum (d - d_N)^2 \quad (1)$$

$$F_{NN} = W_{NN} \sum (d - d_{NN})^2 \quad (2)$$

The W's are adjustable weights [in the range of 10–30 kcal/(mol·Å^2)], d is the current value of the interproton distance, d_N is a target upper bound, and d_{NN} is a target lower bound. Equation 1 is implemented when d is greater than d_N, and eq 2 is implemented when d is less than d_{NN}. All penalty functions were released in the last minimization steps to yield unrestrained final structures that are energy minima. Computations were carried out at the Department of Energy's National Energy Research Supercomputer Center and the National Science Foundation's San Diego Supercomputer Center.

RESULTS

Exchangeable Nucleic Acid Protons. The exchangeable proton spectrum (10.0–15.0 ppm) of the (+)-*trans-anti*-[BPh]-dA·dT 11-mer duplex in H_2O buffer, pH 7.0, at 1 °C is plotted in Figure 1A. The imino protons are well resolved in this spectrum, and we also detect exchangeable resonances between 11.15 and 12.0 ppm which are to high field of the normal imino proton spectral dispersion (Figure 1A). The imino protons have been assigned following analysis of the 150-ms-mixing-time NOESY spectrum of the adduct duplex **3** in H_2O buffer solution at 1 °C. We can monitor NOEs between imino protons on adjacent base pairs along the length of the adduct duplex, and these are traced in the expanded NOESY contour plot of the symmetrical 11.0–14.5 ppm region in Figure 2A. This tracing can be readily followed from the imino proton of dT2 positioned toward one end of the helix to the imino proton of dG13 positioned toward the other end of the helix, except for a missing NOE (see box, Figure 2A) between the imino protons of dT17 (12.0 ppm) and dG18 (11.15 ppm), which are shifted significantly to high field.

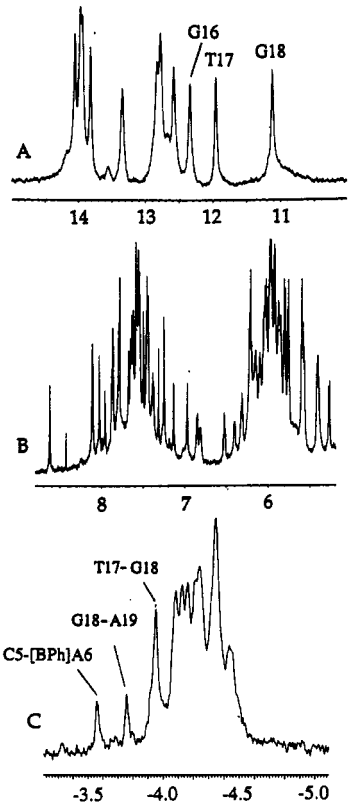

FIGURE 1: (A) Imino proton spectrum (10.0–15.0 ppm) in H_2O buffer at 1 °C, (B) nonexchangeable proton spectrum (5.2–8.8 ppm) in D_2O buffer at 25 °C, and (C) proton-decoupled phosphorus spectrum (–3.0 to –5.0 ppm) in D_2O buffer at 25 °C of the (+)-*trans-anti*-[BPh]dA·dT 11-mer duplex. The buffer was 0.1 M NaCl and 10 mM phosphate, aqueous solution, pH 7.0. Selective imino proton assignments are recorded over the spectrum in (A), and selective phosphorus assignments are recorded over the spectrum in (C).

An expanded NOESY contour plot correlating the NOEs between the imino protons (11.0–14.5 ppm) and the base and amino protons (5.2–8.5 ppm) is plotted in Figure 2B. The observed NOE patterns establish Watson–Crick pairing at all dG·dC base pairs on the basis of NOEs between the deoxyguanosine imino protons and the deoxycytidine amino protons across the base pair, as shown for the dC7·dG16 (peaks A and A′, Figure 2B) and dC5·dG18 pairs (peaks B and B′, Figure 2B) which flank the lesion site. The observed NOE patterns also establish Watson–Crick pairing at all unmodified dA·dT base pairs on the basis of NOEs between the thymidine imino protons and the deoxyadenosine H2 and amino protons across the base pair. More importantly, the imino proton of dT17 exhibits characteristic medium-intensity NOEs to the H2 (peak D, Figure 2B) and NH-6 protons (peak C, Figure 2B) of [BPh]dA6 across the pair, establishing formation of an intact Watson–Crick [BPh]dA6·dT17 base pair at the lesion site. In addition, NOEs are detected between the imino proton of dG16 and the H2 (medium-intensity peak F, Figure 2B) and NH-6 protons (weak intensity peak E, Figure 2B) of [BPh]dA6, establishing that the dC7·dG16 and [BPh]-dA6·dT17 base pairs are stacked on each other. By contrast, we do not detect NOEs between protons on the dC5·dG18 base pair and protons on the [BPh]dA6·dT17 base pair in the imino proton to base and amino proton region of the NOESY spectrum (Figure 2B) even though these base pairs are adjacent to each other in the sequence of adduct duplex **3**.

The exchangeable imino and amino proton chemical shifts for the central d(C5-[BPh]A6-C7)·d(G16-T17-G18) segment are listed in Table I. We have also compared the corresponding proton shifts between the adduct duplex **3** and the control duplex, and the chemical shift differences are listed in Table S1 (supplementary material). Large upfield shifts ranging between +1.3 and +1.6 ppm are detected at the imino protons of dG18 and dT17 and the hydrogen-bonded and exposed amino protons of dC5 on adduct formation.

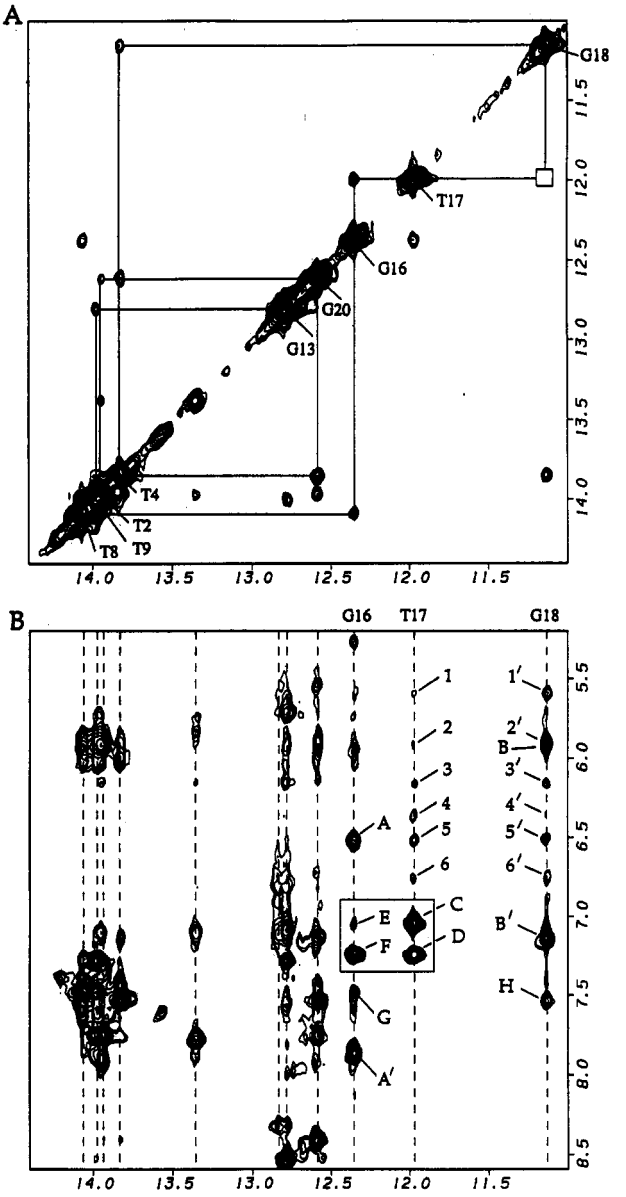

FIGURE 2: Expanded NOESY (150-ms mixing time) contour plots of the (+)-*trans-anti*-[BPh]dA·dT 11-mer duplex in H_2O buffer at 1 °C. (A) NOE connectivities in the symmetrical 11.0–14.5 ppm region. The imino proton assignments are labeled along the diagonal. The lines trace the NOE connectivities between adjacent base pairs starting at dT2 toward one end of the helix and proceeding to dG13 toward the other end of the helix. Note that no NOE connectivity is detected between the imino protons of adjacent dT17 and dG18 (boxed region). (B) NOE connectivities between the imino protons (11.0–14.5 ppm) and the base and amino protons (5.0–8.5 ppm). The NOE cross peaks involving the imino protons of dG16, dT17, and dG18 centered about the lesion site are labeled in the figure. The cross peaks A–H are assigned as follows: A, A′, G16(NH1)–C7-(NH_2-4b,e); B, B′, G18(NH1)–C5(NH_2-4b,e); C, T17(NH3)–A6-(NH6); D, T17(NH3)–A6(H2); E, G16(NH1)–A6(NH6); F, G16(NH1)–A6(H2); G, G16(NH1)–A15(H2); H, G18(NH1)–A19-(H2)/BPh(H6). The peaks 1–6 and 1′–6′ are assigned as follows: 1, T17(NH3)–BPh(H11); 2, T17(NH3)–BPh(H8); 3, T17(NH3)–BPh(H9); 4, T17(NH3)–BPh(H1); 5, T17(NH3)–BPh(H10); 6, T17-(NH3)–BPh(H12); 1′, G18(NH1)–BPh(H11); 2′, G18(NH1)–BPh(H8); 3′, G18(NH1)–BPh(H9); 4′, G18(NH1)–BPh(H1); 5′, G18(NH1)–BPh(H10); 6′, G18(NH1)–BPh(H12).

Nonexchangeable Nucleic Acid Protons. We observe well-resolved nonexchangeable proton spectra (5.0–9.0 ppm) for

Table I: Proton Chemical Shifts of the d(C5-[BPh]A6-C7)·d(G16-T17-G18) Segment of the (+)-*trans-anti*-[BPh]dA·dT 11-mer Duplex in Aqueous Buffer

Exchangeable Proton Chemical Shifts, ppm, 1 °C				
bases	G(NH1)	T(NH3)	C(NH_2-4)	A(NH_2-6)
dC5·dG18	11.15		5.91, 7.11	
[BPh]dA6·dT17		11.99		7.07
dC7·dG16	12.35		6.53, 7.87	

Nonexchangeable Proton Chemical Shifts, ppm, 25 °C						
base	H8/H6	H2/H5/CH_3	H1′	H2′, 2″	H3′	H4′
dC5	7.38	5.10	5.75	2.18, 2.48	5.01	4.25
[BPh]dA6	8.62	7.25	6.31	2.81, 2.91	5.09	4.50
dC7	7.44	5.27	5.98	(2.19), 2.47	4.79	4.27
dG16	7.25		5.57	2.04, 2.31	4.77	4.17
dT17	6.97	0.94	5.98	2.16, 2.10	4.84	4.10
dG18	7.95		5.13	2.63, 2.63	4.88	4.24

the (+)-*trans-anti*-[BPh]dA·dT 11-mer duplex in D_2O buffer at 25 °C (Figure 1B). Nonexchangeable proton assignments were based on an analysis of through-space distance connectivities in NOESY data sets recorded as a function of mixing time and through-bond connectivities in COSY, DQF-COSY, and HOHAHA data sets in D_2O buffer at 25 °C. Expanded NOESY (300-ms mixing time) contour plots of the base (6.9–8.7 ppm) to sugar H1′ and cytidine H5 (5.0–6.4 ppm) regions are shown in duplicate in Figure 3. The base proton to its own and 5′-flanking sugar H1′ proton connectivities are traced from dC3 to dT9 for the modified strand in Figure 3A and from dA14 to dG20 for the unmodified strand in Figure 3B. We note that the NOE cross peak between the H8 proton of dG18 and the H1′ proton of dT17 is missing (see box, Figure 3B) at the dT17–dG18 step.

These base and sugar H1′ proton assignments have been confirmed by cross checks in other regions of the NOESY plot which also have yielded a complete set of sugar H2′, H2″, and H3′ proton assignments. The nonexchangeable proton chemical shifts for the central d(C5-[BPh]A6-C7)·d(G16-T17-G18) segment are listed in Table I. We have also compared the corresponding proton shifts between the adduct duplex **3** and the control duplex, and the estimated chemical shift differences are listed in Table S1 (supplementary material). We detect a moderate upfield shift at the H5 of dC5 (+0.75 ppm) and a smaller upfield shift at the CH_3 of dT17 (+0.24 ppm) and a downfield shift at the H8 of [BPh]-dA6 (–0.37ppm) on adduct formation.

Nonexchangeable Benzo[c]phenanthrene Protons. The nonexchangeable benzo[*c*]phenanthrene protons were assigned from an analysis of the through-bond and through-space connectivities in the (+)-*trans-anti*-[BPh]dA·dT 11-mer duplex and are plotted in Figure S3 (supplementary material) and tabulated in the caption to Figure 4. The aromatic phenanthrenyl ring protons could be readily assigned, while those of the benzylic ring were less straightforward. The latter complications arose because the BPh(H2)–BPh(H3) cross peak was close to the diagonal, while the BPh(H3)–BPh(H4) cross peak overlapped with sugar H3′–H4′ cross peaks. We were able to overcome these difficulties by recording TOCSY spectra as a function of spin-lock time where the coupling connectivities could be relayed along the BPh(H1)–BPh(H2)–BPh(H3)–BPh(H4) segment of the benzylic ring at longer spin-lock times (Figure S4, supplementary material).

The phenanthrenyl ring protons of benzo[*c*]phenanthrene should resonate between 8.0 and 8.5 ppm in protected [BPh]-dA adducts (Agarwal et al., 1987), but they are all shifted to high field in the (+)-*trans-anti*-[BPh]dA·dT 11-mer duplex (Figure S3). The largest upfield shifts are detected for the

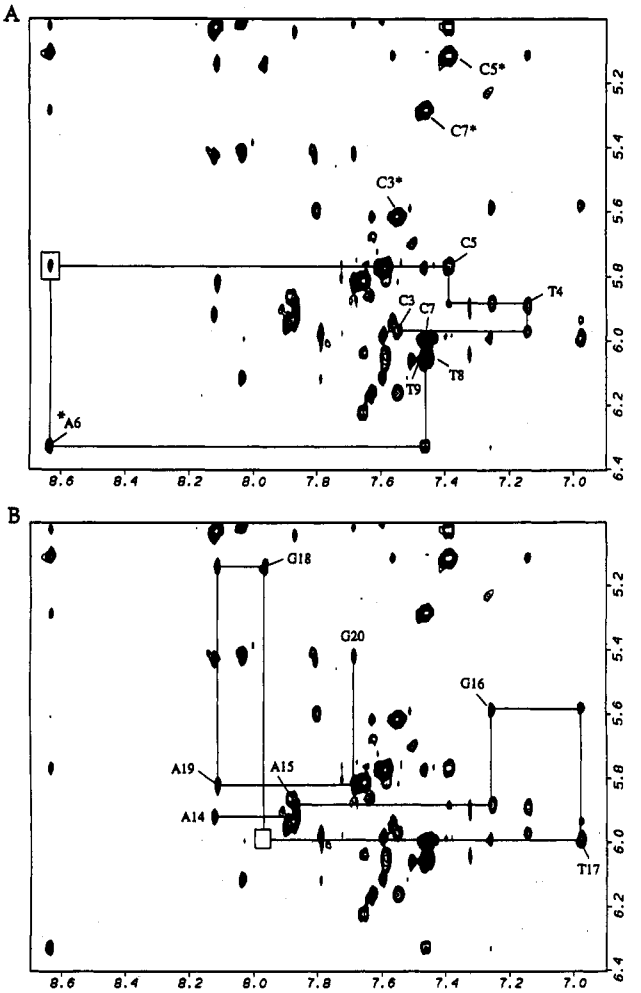

FIGURE 3: Duplicated expanded NOESY (300-ms mixing time) contour plots of the (+)-*trans-anti*-[BPh]dA·dT 11-mer duplex in D_2O buffer at 25 °C establishing distance connectivities between the base (purine H8 and pyrimidine H6) protons (6.9–8.7 ppm) and the sugar H1′ and deoxycytidine H5 protons (4.9–6.4 ppm). (A) NOE connectivities between the bases and their own and 5′-flanking sugar H1′ protons from dC3 to dT9 on the modified strand. The assignments label the base to their own sugar H1′ NOEs, while the deoxycytidine H6–H5 NOEs are designated by asterisks. The somewhat weakened NOE between the H8 of [BPh]dA6 and the H1′ of dC5 is boxed. (B) NOE connectivities between the bases and their own and 5′-flanking sugar H1′ protons from dA14 to dG20 on the unmodified strand. The absent NOE between the H8 of dG18 and the H1′ of dT17 is boxed.

benzo[*c*]phenanthrene H7, H8, H9, H10, H11, and H12 protons.

The experimental coupling cross peaks BPh(H1)–BPh(H2) and BPh(H3)–BPh(H4) are well resolved in the phase-sensitive COSY spectrum, and there is good agreement between these experimental cross-peak patterns and their simulated counterparts based on three-bond vicinal proton–proton coupling constant values of ^3J(H1,H2) = 8.1 ± 0.9 Hz, ^3J(H2,H3) = 2.5 ± 0.5 Hz, and ^3J(H3,H4) = 4.8 ± 0.5 Hz. These coupling constant values are consistent with the distorted half-chair conformation of the benzylic ring where the BPh(H1) and BPh(H2) protons adopt pseudodiaxial orientations while the BPh(H3) and BPh(H4) protons adopt pseudodiequatorial orientations.

Intermolecular NOEs. A set of intermolecular NOEs between nonexchangeable BPh protons and exchangeable and nonexchangeable nucleic acid protons have been identified and assigned in the (+)-*trans-anti*-[BPh]dA·dT 11-mer duplex. Several of these intermolecular NOEs are labeled by numbers in the expanded NOESY (150-ms mixing time) contour plot of exchangeable protons in H_2O solution (Figure

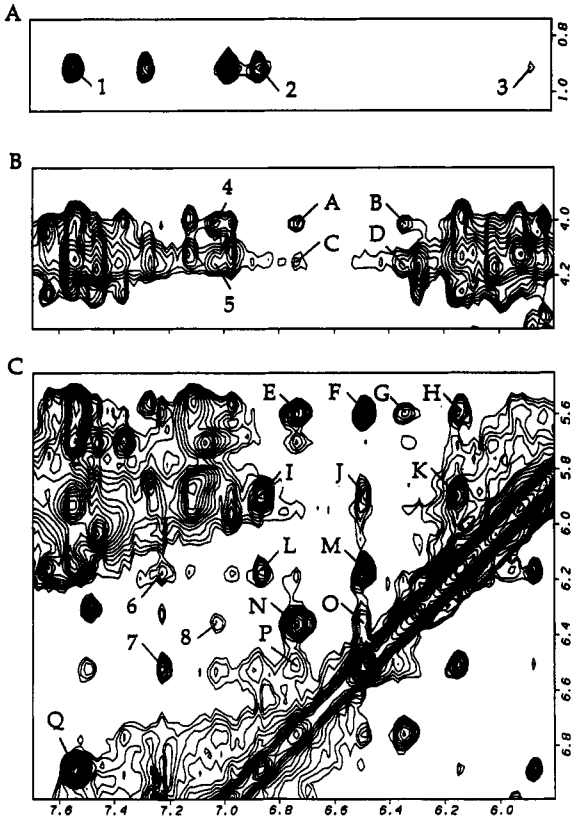

FIGURE 4: Expanded NOESY (150-ms mixing time) contour plots of the (+)-*trans-anti*-[BPh]dA·dT 11-mer duplex in H_2O buffer at 1 °C. The cross peaks labeled 1–8 identify intermolecular NOEs between the benzo[*c*]phenanthrene protons and the DNA protons and are assigned as follows: 1, BPh(H6)–T17(CH_3); 2, BPh(H7)–T17(CH_3); 3, BPh(H8)–T17(CH_3); 4, BPh(H2)–[BPh]A6(NH6); 5, BPh(H3)–[BPh]A6(NH6); 6, BPh(H9)–[BPh]A6(H2); 7, BPh(H10)–[BPh]A6(H2); 8, BPh(H1)–[BPh]A6(NH6). The cross peaks labeled A–Q identify NOEs among benzo[*c*]phenanthrene protons and are assigned as follows: A, BPh(H2)–BPh(H12); B, BPh(H1)–BPh(H2); C, BPh(H3)–BPh(H12); D, BPh(H1)–BPh(H3); E, BPh(H11)–BPh(H12); F, BPh(H10)–BPh(H11); G, BPh(H1)–BPh(H11); H, BPh(H9)–BPh(H11); I, BPh(H7)–BPh(H8); J, BPh(H8)–BPh(H10); K, BPh(H8)–BPh(H9); L, BPh(H7)–BPh(H9); M, BPh(H9)–BPh(H10); N, BPh(H1)–BPh(H12); O, BPh(H1)–BPh(H10); P, BPh(H10)–BPh(H12); Q, BPh(H6)–BPh(H7). The chemical shift values for the benzylic protons are BPh(H1), 6.40 ppm; BPh(H2), 4.06 ppm; BPh(H3), 4.13 ppm; and BPh(H4), 4.94 ppm. The chemical shift values for the phenanthrenyl protons are BPh(H5), 7.57 ppm; BPh (H6), 7.56 ppm; BPh(H7), 6.85 ppm; BPh(H8), 5.93 ppm; BPh(H9), 6.22 ppm; BPh(H10), 6.52 ppm; BPh(H11), 5.59 ppm; and BPh(H12), 6.81 ppm.

2B) and in the expanded NOESY (300-ms mixing time) contour plots of nonexchangeable protons in D_2O buffer (Figure 4), and the cross-peak assignments are listed in the figure captions. The corresponding intermolecular distance constraints defined by lower and upper bounds for the central d(C5-[BPh]A6-C7)·d(G16-T17-G18) segment are listed in Table II.

The distribution of nonexchangeable proton distance constraints is such that they are restricted to intermolecular NOEs between the benzo[*c*]phenanthrene protons of the carcinogen and the dC5·dG18 and [BPh]dA6·dT17 base pairs of the nucleic acid (Table II; Figure 4). A similar observation is made for the distance constraints involving exchangeable protons in that the imino protons of dT17 and dG18 exhibit intermolecular NOEs to a set of benzo[*c*]phenanthrene protons (peaks 1–6 and 1′–6′, Figure 2B) in adduct duplex **3**.

The combined pattern of specific intermolecular NOEs (Table II) and upfield proton chemical shifts (Table S1; Figure S3) presented above establishes unambiguously that the benzo-

Table II: Comparison of Input Interproton Distance Bounds with Those Observed for the Lowest Energy Solution Structure of the (+)-*trans-anti*-[BPh]dA·dT 11-mer Duplex

	interproton distances, Å	
	exptl bounds	obsd
exchangeable protons (intramolecular)		
G16(NH1)–[BPh]A6(NH6)	3.0–5.0	4.34
G16(NH1)–[BPh]A6(H2)	2.0–3.5	2.72
T17(NH3)–[BPh]A6(NH6)	2.6–3.0	2.26
T17(NH3)–[BPh]A6(H2)	2.8–3.3	3.19
exchangeable protons (intermolecular)		
[BPh]A6(NH6)–BPh(H1)	3.0–5.0	3.07
[BPh]A6(NH6)–BPh(H2)	2.5–4.5	2.70
[BPh]A6(NH6)–BPh(H3)	3.0–5.0	5.03
nonexchangeable protons (intermolecular)		
C5(H1′)–BPh(H11)	3.0–5.0	5.02
C5(H1′)–BPh(H12)	3.0–5.0	4.40
C5(H1′)–BPh(H1)	3.5–5.5	4.45
C5(H2′,H2″)–BPh(H12)	3.0–5.0	5.21, 4.62
C5(H2′,H2″)–BPh(H1)	3.0–5.0	4.12, 3.63
C5(H5)–BPh(H12)	4.0–6.0	5.13
[BPh]A6(H8)–BPh(H1)	4.0–6.0	4.22
[BPh]A6(H8)–BPh(H11)	4.0–6.0	4.98
[BPh]A6(H2)–BPh(H10)	3.0–5.0	4.07
[BPh]A6(H2)–BPh(H9)	4.0–6.0	5.38
T17(H6)–BPh(H8)	3.0–5.0	3.29
T17(H6)–BPh(H7)	4.0–6.0	4.35
T17(CH_3)–BPh(H6)	2.0–4.0	3.59
T17(CH_3)–BPh(H7)	3.0–5.0	3.16
T17(CH_3)–BPh(H8)	4.0–6.0	4.25

[*c*]phenanthrene ring which is covalently linked to the N^6 of dA6 is intercalated between the dC5·dG18 and [BPh]dA6·dT17 base pairs in (+)-*trans-anti*-[BPh]dA·dT 11-mer duplex **3**.

Phosphorus Spectra. The proton-decoupled phosphorus spectrum of the (+)-*trans-anti*-[BPh]dA·dT 11-mer duplex in D_2O buffer at 25 °C exhibits two downfield-shifted phosphorus resonances which are outside the –4.0 to –4.5 ppm spectral region characteristic of unperturbed phosphodiester backbones (Figure 1C). The phosphorus resonances have been assigned from an analysis of a proton–phosphorus heteronuclear correlation experiment with the expanded contour plot shown in Figure 5. Each nonterminal phosphorus can be correlated with its 5′-linked H3′ proton (three-bond H–P coupling) and its 3′-linked H4′ proton (four-bond H–P coupling), and the phosphorus resonances can be assigned on the basis of the known sugar H3′ and H4′ proton assignments. The most downfield shifted phosphorus at –3.18 ppm is assigned to the dC5–[BPh]dA6 step, while the next most downfield phosphorus at –3.39 ppm is assigned to the dG18–dA19 step in the (+)-*trans-anti*-[BPh]dA·dT 11-mer duplex (Figure 5).

Energy Minimization Computations. The search strategy employed in the present work began with a B-DNA (Arnott et al., 1976) central three-base-pair d(C5-[BPh]A6-C7)·d(G16-T17-G18) segment of the (+)-*trans-anti*-[BPh]dA·dT 11-mer duplex. The two [BPh]dA structures with different benzylic ring puckers that had been energy minimized with MacroModel (see Materials and Methods) were inserted into this trinucleotide duplex segment. For each of these trinucleotide segments, the BPh–DNA orientation space was searched with 16 energy minimization trials in which α' [dA6-(N^1)-dA6(C^6)-dA6(N^6)-BPh(C^1)] and β' [dA6(C^6)-dA6-(N^6)-BPh(C^1)-BPh(C^2)] were each started at 0°, 90°, 180°, and 270° in all combinations and the DNA starting conformation was the B-form.

In these trials, the DUPLEX hydrogen bond penalty function (Hingerty et al., 1989) for Watson–Crick base pairing was utilized at all base pairs since the NMR data indicated

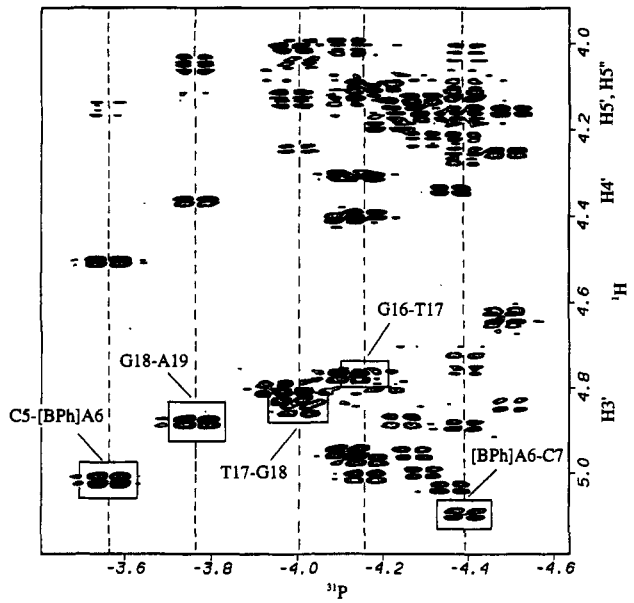

FIGURE 5: An expanded contour plot of the proton-detected phosphorus–proton heteronuclear correlation experiment on the (+)-*trans-anti*-[BPh]dA·dT 11-mer duplex in D_2O buffer at 25 °C. The phosphorus assignments for steps centered about the lesion site are listed. The correlation cross peaks between the phosphorus and its 5′-linked sugar H3′ protons are boxed.

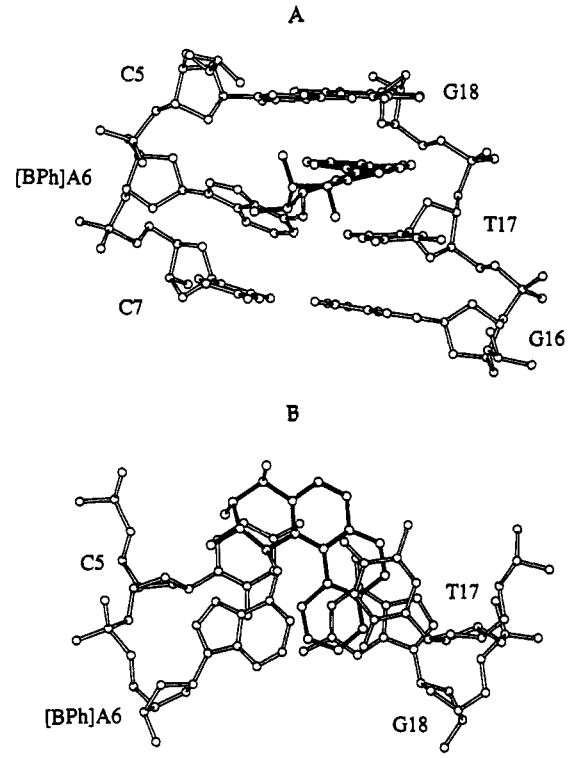

FIGURE 6: (A) A view looking into the major groove and normal to the helix axis of the solution structure of the d(C5-[BPh]A6-C7)·d(G16-T17-G18) segment of the (+)-*trans-anti*-[BPh]dA·dT 11-mer duplex. The B[*c*]Ph ring system is shown in darkened bonds and is intercalated between the dC5·dG18 and [BPh]dA6·dT17 base pairs. (B) A view looking down the helix axis for the d(C5-[BPh]A6)·d(T17-G18) segment of the solution structure of the (+)-*trans-anti*-[BPh]dA·dT 11-mer duplex. Note that the benzylic ring is in the major groove while the phenanthrene ring of [BPh]dA6 overlaps with the NH_2 group of dC5 and the hydrogen-bonding edges of dT17 and dG18. These drawings were prepared using MolScript V1.1 (Kraulis, 1991).

that the modified base pair was hydrogen-bonded, and the NMR-derived upper- and lower-bound distance restraints listed in Table II were included. Searching orientation space at 90° intervals of α' and β' is a robust procedure for locating all the important potential energy wells because our minimization protocol permits torsion angle variations up to 100° in each minimization step (Hingerty et al., 1989). Consequently, energy minima in each quadrant of α' and β' are accessible, and the reduced-variable domain of torsion angle space greatly enhances the likelihood of finding the important structures.

These computations identified the family of structures in which the benzo[*c*]phenanthrene ring of the (+)-*trans-anti*-[BPh]dA adduct intercalates in the 5′-direction and is sandwiched between intact Watson–Crick dC5·dG18 and [BPh]dA6·dT17 base pairs. The results of the two sets of searches on the d(C5-[BPh]A6-C7)·d(G16-T17-G18) segment clearly revealed that the benzylic ring conformation with the BPh(H1) and BPh(H2) protons in pseudodiaxial orientations and the BPh(H3) and BPh(H4) protons pseudodiequatorial is preferred. The lowest energy structure of the trinucleotide segment with this conformation had an energy of −116.4 kcal/mol and goodness of fit values for eqs 1 and 2 of 0.006 and 17.3, respectively, with W = 15 kcal/(mol·Å^2). Of the 16 structures, a second was nearly identical to this form and six others were similar in overall aspect. By contrast, the best structure of the trinucleotide segment from the search with BPh(H1) and BPh(H2) in pseudodiequatorial orientations and with the BPh(H3) and BPh(H4) protons pseudodiaxial had an energy of −83.0 kcal/mol with goodness of fit values of 14.4 and 46.3, respectively, with W = 15 kcal/(mol·Å^2). Consequently, the lowest energy trinucleotide segment with the former benzylic ring pucker was embedded in an energy-minimized B-form 11-mer and reminimized with all restraints. Subsequently the hydrogen bond penalty function and the distance restraints were released with energy minimization in one step, yielding a final unrestrained structure.

Solution Structure. A view normal to the helix axis and looking into the major groove for the central d(C5-[BPh]-A6-C7)·d(G16-T17-G18) segment of the lowest energy NMR–energy-minimized structure of the (+)-*trans-anti*-[BPh]dA·dT 11-mer duplex is shown in Figure 6A. The benzo[*c*]phenanthrene moiety which is covalently linked to the major groove N^6 of dA6 intercalates to the 5′-side of the modification site without disruption of the modified base pair. The dC5·dG18 and [BPh]dA6·dT17 base pairs which flank the intercalation site adopt Watson–Crick pairing alignments. We note that the [BPh]dA6·dT17 pair is propeller-twisted by 15° [computed using the approach of Babcock and Olson (1993)] with the minor groove edge of [BPh]dA6 tipped toward the flanking dC7·dG16 base pair. The intercalation site is wedge-shaped at the dC5–[BPh]dA6 step, while the dT17 and dG18 bases are parallel to each other at the dT17–dG18 step. The phenanthrenyl chromophore overlaps with the hydrogen-bonding edges of dT17 and dG18 bases at the dT17–dG18 step on the unmodified strand as seen in a view down the helix axis for the segment d(C5-[BPh]A6)·d(T17-G18) in the NMR–energy-minimized structure (Figure 6B). This alignment positions the nonplanar benzylic ring of BPh in the major groove with the phenanthrenyl ring inserting into the intercalation site but not penetrating through into the minor groove (Figure 6B).

The benzylic ring of BPh adopts a distorted half-chair conformation with the BPh(H1) and BPh(H2) protons in pseudodiaxial orientations while the BPh(H3) and BPh(H4) protons adopt pseudodiequatorial orientations. The potential steric clash between the BPh(H1) and BPh(H12) protons is relieved by a propeller-like distortion of the aromatic phenanthrenyl ring away from planarity in the solution structure of the adduct duplex (Figure 6A). This distortion away from

planarity is defined by the dihedral angle C4B–C6B–C8B–C12, which adopts a value of 18.1°.

The carcinogen–base linkage site for the [BPh]dA6 residue is defined by the angles α' [dA6(N^1)-dA6(C^6)-dA6(N^6)-BPh(C^1)] = 153° and β' [dA6(C^6)-dA6(N^6)-BPh(C^1)-BPh(C^2)] = 104° in the NMR–energy-minimized structure of the (+)-*trans-anti*-[BPh]dA·dT 11-mer duplex. The glycosidic torsion angles, sugar puckers, and backbone torsion angles for the d(C5-[BP]A6-C7)·d(G16-T17-G18) segment of the (+)-*trans-anti*-[BPh]dA·dT 11-mer duplex are listed in Table S2 (supplementary material). Interestingly, except for the sugar pucker of dT17, all backbone torsion angles including sugar pseudorotation parameters (Altona & Sundaralingam, 1972) fall in, or very near, the B_I-DNA conformation on formation of an intercalation site at the d(C5-[BPh]A6)·d(T17-G18) step.

Convergence to very similar final structures resulted when the lowest energy NMR energy-minimized structure was distorted by +45° or –45° at each of the two bonds (α' and β') at the base–carcinogen linkage and reminimized with restraints. Two views of the best-fit superposition of the resulting four structures are plotted in Figure S5 (supplementary material). These views provide an estimate of the precision to which we can define the geometry of the intercalation site, the position of the modified dA6 and its opposing dT17, and the overlap geometry between the pyrenyl ring and the flanking base pairs.

DISCUSSION

Spectral Quality. We observe reasonably well resolved imino (Figure 1A) and nonexchangeable proton resonances (Figure 1B) and partially resolved phosphorus resonances (Figure 1C) for the (+)-*trans-anti*-[BPh]dA·dT 11-mer duplex. This is especially true for protons in the d(C5-[BPh]-A6-C7)·d(G16-T17-G18) segment which is centered about the adduct site. Thus, the imino protons of dG16, dT17, and dG18 both are well resolved and exchange slowly so that the NOEs from these protons map out the immediate vicinity of the lesion site. Further, there exists a single predominant alignment for (+)-*trans-anti*-[BPh]dA positioned opposite dT in the 11-mer duplex on the basis of the proton spectra (Figure 1A,B), and this conclusion is verified by the absence of exchange cross peaks in the NOESY spectrum, which would be indicative of a second form in slow equilibrium.

The NOE connectivities involving exchangeable protons (Figure 2) and nonexchangeable protons (Figure 3) can be readily followed in the NOESY data sets, thus permitting the assignment of nucleic acid (Table I) and carcinogen protons (Figure S3) in the adduct duplex. Further, deviations from expected NOE patterns readily identify the sites of structural distortions in the DNA helix (Figures 2 and 3). We have been able to identify a series of well-resolved intermolecular NOEs between the benzo[*c*]phenanthrene and nucleic acid protons (numbered cross peaks in Figures 2 and 4) that provide the constraints (Table II) to align the carcinogen along the helix.

Base Pairing at the Intercalation Site. The intercalation site is generated without disruption of the dC5·dG18 and [BPh]-dA6·dT17 base pairs that flank it. These pairs adopt Watson–Crick alignments on the basis of the characteristic NOEs across the pairs which define this alignment, as do all other pairs in the (+)-*trans-anti*-[BPh]dA·dT 11-mer duplex. However, the [BPh]dA6·dT17 pair is propeller-twisted such that the minor groove H2 proton containing edge of [BPh]-dA6 is closer to the adjacent dC7·dG16 base pair (Figure 6A). This propeller-twist orientation reflects the experimental observation of a stronger NOE from the imino protons of dG16 to the minor groove H2 proton (peak F, Figure 2B) relative to the major groove NH-6 proton (peak E, Figure 2B) of [BPh]dA6 for adduct duplex **3**. The deoxyadenosine amino proton at the covalent linkage site is also out of the plane of the dA6 ring, which in turn orients the dA6(N^6)–BPh(C^1) linkage bond to facilitate intercalation of the benzo[*c*]-phenanthrene ring into the helix.

Intercalation Site Geometry. The intercalation site is buckled in the NMR energy-minimized structure (Figure 6A) such that dT17 and dG18 are parallel to each other (and hence their protons are further apart) while dC5 and [BPh]-dA6 are wedge-shaped (and hence their protons are closer to each other). This greater separation at the dT17–dG18 step results from the phenanthrenyl chromophore being sandwiched predominantly between the dT17 and dG18 bases on the unmodified strand (Figure 6B). This buckled geometry at the intercalation site is experimentally supported by the absence of an NOE between the H8 proton of dG18 and the H1′ proton of dT17 (see box, Figure 3B) at the dT17–dG18 step, in contrast to the dC5–[BPh]dA6 step where an NOE is detected between the H8 proton of [BPh]dA6 and the H1′ proton of dC5 (see box, Figure 3A) in adduct duplex **3**.

There is also a shearing of the base pairs flanking the intercalation site with dT17 and dG18 on the unmodified strand stacked more directly over each other and over the intercalated phenanthrenyl ring, in contrast to dC5 and [BPh]dA6 on the modified strand, which do not stack over each other or with the intercalated phenanthrenyl ring (Figure 5B).

The intercalation site in the NMR energy-minimized structure contains a C4′-*exo*/O1′-*endo* sugar pucker at dT17 while retaining all other backbone torsion angles in or very near the B family of DNA conformations (Drew et al., 1981) (Table S2).

Stacking at the Intercalation Site. The intercalation of the benzo[*c*]phenanthrene ring between the dC5·dG18 and [BPh]dA6·dT17 base pairs in the NMR–energy-minimized structure of the (+)-*trans-anti*-[BPh]dA·dT 11-mer duplex (Figure 6B) should result in novel NOE and chemical shift patterns with the structure satisfying not only the distance constraints but also the observed chemical shift changes in the carcinogen and nucleic acid protons on adduct formation.

The benzylic ring is positioned in the major groove and partially stacks over dC5 on the modified strand while the long axis of the phenanthrenyl ring is normal to the long axis of the flanking base pairs such that two of its aromatic rings stack over dT17 and dG18 on the unmodified strand (Figure 6B). Interestingly, there is no stacking detected between the benzo[*c*]phenanthrene ring and its attached modified dA6 base. This stacking geometry which precisely positions the edges of the carcinogen and the base pairs (Figure 6B) is supported by the observed pattern of intermolecular NOEs between the benzo[*c*]phenanthrene ring protons and the protons on the d(C5-[BPh]A6)·d(T17-G18) segment at the intercalation site (Table II). The benzylic BPh(H1) and phenanthrenyl BPh(H11) and BPh(H12) protons that lie on one edge of the BPh ring system exhibit NOEs to the sugar H1′ and H2′/H2″ protons of dC5 and the H8 proton of [BPh]-dA6 on the modified strand of the adduct duplex. The phenanthrenyl BPh(H6), BPh(H7), and BPh(H8) protons on the opposite edge of the BPh ring system exhibit NOEs to the major groove H6 and CH_3 protons of dT17 on the unmodified complementary strand of the adduct duplex (peaks 1, 2, and 3, respectively, of Figure 4A). The phenanthrenyl BPh(H9) and BPh(H10) protons located on another BPh edge exhibit NOEs to the minor groove H2 proton of [BPh]dA6 in the

adduct duplex (peaks 6 and 7, respectively, of Figure 4C). The benzylic BPh(H1), BPh(H2), and BPh(H3) protons exhibit NOEs to the major groove NH-6 amino proton of [BPh]dA6 in the adduct duplex (peak 8, Figure 4C, and peaks 4 and 5, Figure 4B, respectively). We did not detect intermolecular NOEs from the benzylic BPh(H4) and phenanthrenyl BPh(H5) and BPh(H6) protons to the nucleic acid protons, and these observations are consistent with these benzo[*c*]phenanthrenyl protons being furthest away from protons positioned on the base pair edges flanking the bisintercalation site (Figure 6B).

The overlap geometry of the benzo[*c*]phenanthrene ring with flanking dC5·dG18 and [BPh]dA6·dT17 base pairs in the NMR–energy-minimized structure of the (+)-*trans-anti*-[BPh]dA·dT 11-mer duplex is supported not only by the intermolecular nonexchangeable proton NOEs outlined above (Table II and Figure 4) but also by the observed NOEs from the imino protons of dT17 and dG18 to the BPh(H11), BPh(H8), BPh(H9), BPh(H1), BPh(H10), and BPh(H12) protons (peaks 1–6 and 1′–6′, Figure 2B). These latter observations are consistent with the phenanthrenyl ring protons extending from BPh(H8) to BPh(H12) and the benzylic ring BPh(H1) proton being closer to the helix axis relative to the benzo[*c*]phenanthrenyl ring protons extending from BPh(H2) to BPh(H6) in the adduct duplex (Figure 6B).

The stacking geometry between the phenanthrenyl ring and the flanking base pairs at the intercalation site (Figure 6B) readily accounts for the large upfield shifts detected for the carcinogen and nucleic acid protons on proceeding from the control duplex to the (+)-*trans-anti*-[BPh]dA·dT 11-mer duplex (Table S1). Thus, the imino protons of dT17 and dG18 which are positioned directly over the phenanthrenyl aromatic ring furthest from the covalent linkage site (Figure 6B) are predicted to undergo large upfield shifts, which have been observed experimentally (+1.53 ppm for dT17 and +1.38 ppm for dG18; Table S1). Similarly, both amino protons of dC5 are positioned over the phenanthrenyl ring closest to the covalent linkage site (Figure 6B), and the expected upfield shifts for these amino protons are also observed experimentally (upfield shifts of +1.61 and +1.35 ppm). The H5 of dC5 is stacked over the nonaromatic benzylic ring (Figure 6B) but still shifts upfield by +0.75 ppm on formation of the adduct duplex **3**.

We have pointed out that all the phenanthrenyl ring protons are shifted upfield on formation of adduct duplex **3** (Figure S3) in contrast to their unperturbed chemical shift values in the 8.0–8.5 ppm range. There are distinctions, however, in that the BPh(H5) and BPh(H6) protons undergo the smallest upfield shifts in contrast to the remaining phenanthrenyl ring protons extending from BPh(H7) to BPh(H12), which undergo much larger upfield shifts (Figure S3). This readily follows from the stacking geometry between the phenanthrenyl ring and the flanking base pairs at the intercalation site (Figure 6B) since BPh(H5) and BPh(H6) are furthest from the helix axis while BPh(H7), BPh(H8), BPh(H9), BPh(H10), BPh(H11), and BPh(H12) are closer to the helix axis and experience the upfield ring current shifts from the flanking base pairs.

Intercalation to the 5′-Side of the Adduct Site. A key structural conclusion of the NMR energy-minimized structure of the (+)-*trans-anti*-[BPh]dA·dT 11-mer duplex is the intercalation of the covalently attached benzo[*c*]phenanthrenyl ring 5′ to the [BPh]dA adduct site. It is of interest to understand how both covalent adduct formation and intercalation are achieved without disruption of the modified base pair. The key contributors are likely to be the orientation of the covalent linkage bond, the pucker of the benzylic ring, and deviations from planarity of the phenanthrenyl ring, together with small concerted torsion movements about B-DNA values.

The dA6(N^6)–BPh(C^1) bond is out of the plane of the dA6 ring and directed toward the dC5·dG18 base pair, and it contributes, in part, to bridging the gap between the covalent linkage and intercalation sites. The benzylic ring position is defined by the torsion angles about the dA6(C^6)–dA6(N^6) and dA6(N^6)–BPh(C^1) single bonds, which adopt values of $\alpha' = 154°$ and $\beta' = 104°$, respectively (see Results for the definitions of α' and β').

The preferred half-chair orientation of the benzylic ring pucker in the NMR energy-minimized structure which places the BPh(H1) and BPh(H2) protons in pseudodiaxial positions and the BPh(H3) and BPh(H4) protons in pseudodiequatorial positions is directly supported by the experimental coupling constant data. We detect coupling cross peaks for both the BPh(H1)–BPh(H2) and BPh(H3)–BPh(H4) proton pairs, but the former cross peak [^3J(H1,H2) = 8.1 ± 0.9 Hz] is stronger than the latter [^3J(H3,H4) = 4.8 ± 0.5 Hz], which is indicative of a larger coupling constant expected for a *trans* alignment of protons characteristic of a diaxial orientation. In effect, the pucker of the benzylic ring also contributes to bridging the spacing between the covalent linkage and intercalation sites in adduct duplex **3** (Figure 6A).

The (+)-*trans-anti*-[BPh]dA adduct **2** exhibits a crowded bay region due to the close proximity of the benzylic H1 and phenanthrenyl H12 protons. This crowding is relieved in adduct duplex **3** by the three aromatic phenanthrenyl rings adopting a nonplanar propeller-like orientation (Figure 6A) such that the aromatic ring closest to the covalent linkage site also makes a contribution to bridging the gap between the covalent linkage and intercalation sites. Similar deviations from nonplanarity of the polyene ring have been reported in crystal structures of other polycyclic aromatic hydrocarbons (Zacharias et al., 1984).

Thus, in the (+)-*trans-anti*-[BPh]dA·dT 11-mer duplex, incremental contributions from the linkage bond, the benzylic ring pucker, and the nonplanarity of the phenanthrenyl ring all contribute to the bridging of the space between the covalent linkage site and the intercalation site 5′ to it without disruption of the [BPh]dA·dT base pair. It is worth pointing out that the food mycotoxins aflatoxin and sterigmatocystin bound covalently to the N^7 of deoxyguanosine also intercalate to the 5′-side of the lesion site without disruption of the (MY)dG·dC base pair (Gopalakrishnan et al., 1990, 1992). In this case, the fused bicyclic ring system of the food mycotoxins bridges the covalent linkage and intercalation sites and also orients the aromatic chromophore for intercalation into the helix.

Summary. Our previous NMR–computational research on the solution structure of stereoisomeric benzo[*a*]pyrene–N^2-dG adducts opposite dC at the DNA duplex level has provided the details of carcinogen alignments in groove-binding structures (Cosman et al., 1992; de los Santos et al., 1992) as well as in intercalation with base-displacement structures (Cosman et al., 1993) for this family of polycyclic aromatic hydrocarbon adducts where the covalent linkage is at the minor groove edge of the helix. We were attracted to the challenge of determining the solution structure of related adducts where the covalent linkage is at the major groove edge of the helix and elucidating whether new structural motifs are associated with the switch from covalent linkage at one groove of the helix to the other. This goal was approached through studies of stereoisomeric benzo[*c*]phenanthrene–N^6-dA adducts opposite dT at the duplex level with the present study focused on the (+)-*trans-anti*-[BPh]dA adduct. The resulting NMR

energy-minimization studies establish yet another structural motif where the benzo[*c*]phenanthrene ring intercalates without disruption of the modified base pair. This was an unexpected observation and has provided new insights on the torsion angles about the linkage bonds, the pucker of the benzylic ring, and the nonplanarity of the pyrenyl ring that all combine to position the covalently attached BPh ring for intercalation adjacent and 5′ to the intact modified [BPh]-dA·dT base pair.

ACKNOWLEDGMENT

One of us (S.B.) thanks Prof. James Canary, Chemistry Department, New York University, for assistance with Macromodel.

SUPPLEMENTARY MATERIAL AVAILABLE

Two tables listing proton chemical shift differences on adduct formation (Table S1) and backbone torsion angles of the lowest energy structure for the central trinucleotide segment (Table S2); the five figures, including a partial charge listing for [BPh]dA (Figure S1), two starting structures of [BPh]dA following energy minimization with MacroModel (Figure S2), a plot of the [BPh] ring protons in the adduct duplex (Figure S3), a set of expanded TOCSY spectra of the adduct duplex as a function of spin-lock time (Figure S4), and a superposition of four structures derived following energy minimization with constraints from the lowest energy structure in which the α' and β' angles were changed by $\pm 45°$ (Figure S5) (8 pages). Ordering information is given on any current masthead page.

REFERENCES

Agarwal, S. K., Sayer, J. M., Yeh, H. J. C., Pannell, L. K., Hilton, B. D., Pigott, M. A., Dipple, A., Yagi, H., & Jerina, D. M. (1987) *J. Am. Chem. Soc. 109*, 2497–2504.

Altona, C., & Sundaralingam, M. (1972) *J. Am. Chem. Soc. 94*, 8205–8212.

Arnott, S., Bond, P. J., Selsing, E., & Smith, P. J. (1976) *Nucleic Acids Res. 3*, 2459–2470.

Babcock, M. S., & Olson, W. K. (1993) A new program for the the analysis of nucleic acid structure: Implications for nucleic acid structure interpretation, in *Computation of Biomolecular Structures: Achievements, Problems, Perspectives* (Soumpasis, D. M., & Jovin, T. M., Eds.) Springer Verlag, Heidelberg.

Bigger, C. A. H., Strandberg, J., Yagi, H., Jerina, D. M., & Dipple, A. (1989) *Proc. Natl. Acad. Sci. U.S.A. 86*, 2291–2295.

Bigger, C. A. H., St. John, J., Yagi, H., Jerina, D. M., & Dipple, A. (1992) *Proc. Natl. Acad. Sci. U.S.A. 89*, 368–372.

Canella, K. A., Peltonen, K., Yagi, H., Jerina, D. M., & Dipple, A. (1992) *Chem. Res. Toxicol. 5*, 685–690.

Cheng, S. C., Hilton, B. D., Roman, J. M., & Dipple, A. (1989) *Chem. Res. Toxicol. 2*, 334–340.

Conney, A. H. (1982) *Cancer Res. 42*, 4875–4917.

Cosman, M., Ibanez, V., Geacintov, N. E., & Harvey, R. G. (1990) *Carcinogenesis 11*, 1667–1672.

Cosman, M., de los Santos, C., Fiala, R., Hingerty, B. E., Singh, S., Ibanez, V., Margulis, L., Live, D., Geacintov, N. E., Broyde, S., & Patel, D. J. (1992) *Proc. Natl. Acad. Sci. U.S.A. 89*, 1914–1918.

Cosman, M., de los Santos, C., Fiala, R., Hingerty, B. E., Ibanez, V., Luna, E., Harvey, R., Geacintov, N. E., Broyde, S., & Patel, D. J. (1993) *Biochemistry 32*, 4145–4155.

de los Santos, C., Cosman, M., Fiala, R., Hingerty, B. E., Ibanez, V., Margulis, L., Geacintov, N. E., Broyde, S., & Patel, D. J. (1992) *Biochemistry 31*, 5245–5252.

Dipple, A., Pigott, M. A., Agarwal, S. K., Yagi, H., Sayer, J. M., & Jerina, D. M. (1987) *Nature 327*, 535–536.

Drew, H., Wing, R., Takano, T., Broka, C., Tanaka, S., Itakura, K., & Dickerson, R. E. (1981) *Proc. Natl. Acad. Sci. U.S.A. 78*, 2179–2183.

Gopalakrishnan, S., Harris, T. M., & Stone, M. P. (1990) *Biochemistry 29*, 10438–10448.

Gopalakrishnan, S., Liu, X., & Patel, D. J. (1992) *Biochemistry 31*, 10790–10801.

Hingerty, B. E., & Broyde, S. (1985) *Biopolymers 24*, 2279–2299.

Hingerty, B. E., Figueroa, S., Hayden, T., & Broyde, S. (1989) *Biopolymers 28*, 1195–1222.

Jerina, D. M., Yagi, H., Thakker, D. R., Sayer, J. M., van Bladeren, P. J., Lehr, R. E., Whalen, D. L., Levin, W., Chang, R. L., Wood, A. W., & Conney, A. H. (1984) in *Foreign Compound Metabolism* (Caldwell, J., & Paulson, G. D., Eds.) p 257, Taylor & Francis, London.

Kraulis, P. J. (1991) *J. Appl. Crystallogr. 24*, 946–950.

Levin, W., Chang, R. L., Wood, A. W., Thakker, D. R., Yagi, H., Jerina, D. M., & Conney, A. H. (1986) *Cancer Res. 46*, 2257–2261.

Lunde, G., & Bjorseth, A. (1977) *Nature 268*, 518–519.

Miller, E. C. (1978) *Cancer Res. 38*, 1479–1496.

Misra, B., & Amin, S. (1990) *J. Org. Chem. 55*, 4478–4480.

Mohamadi, F., Richards, N. G., Guida, W. C., Guida, R., Liscamp, R., Caufield, C., Chang, G., Hendrickson, T., & Still, W. C. (1990) *J. Comput. Chem. 11*, 440–467.

Neidle, S., Subbiah, A., Kuroda, R., & Cooper, C. S. (1982) *Cancer Res. 42*, 3766–3768.

Norman, D., Abuaf, P., Hingerty, B. E., Live, D., Grunberger, D., Broyde, S., & Patel, D. J. (1989) *Biochemistry 28*, 7462–7476.

Ornstein, R. L., & Rein, R. (1979) *Biopolymers 18*, 1277–1291.

Patel, D. J., Kozlowski, S. A., Nordheim, A., & Rich, A. (1982) *Proc. Natl. Acad. Sci. U.S.A. 79*, 1413–1417.

Pruess-Schwartz, F., Baird, W. M., Yagi, H., Jerina, D. M., Pigott, M. A., & Dipple, A. (1987) *Cancer Res. 47*, 4032–4037.

Razzel, W. E., & Khorana, H. G. (1961) *J. Biol. Chem. 236*, 1144–1149.

Schlick, T., Hingerty, B. E., Peskin, C. S., Overton, M. L., & Broyde, S. (1990) in *Theoretical Chemistry and Molecular Biophysics* (Beveridge, D., & Lavery, R., Eds.) pp 39–58, Academic Press, New York.

Singer, B., & Grunberger, D. (1983) *Molecular Biology of Mutagens and Carcinogens*, Plenum Press, New York.

Singh, S. B., Hingerty, B. E., Singh, U. C., Greenberg, J. P., Geacintov, N. E., & Broyde, S. (1991) *Cancer Res. 51*, 3482–3492.

Taylor, E. R., & Olson, W. K. (1983) *Biopolymers 22*, 2667–2702.

Thakker, D. R., Levin, W., Yagi, H., Yeh, H. J., Ryan, D. E., Thomas, P. E., Conney, A. H., & Jerina, D. M. (1986) *J. Biol. Chem. 261*, 5404–5413.

van de Ven, F. J., & Hilbers, C. W. (1988) *Eur. J. Biochem. 178*, 1–38.

Wang, A. H. J., Gao, Y. G., Liaw, Y. C., & Li, Y. K. (1991) *Biochemistry 30*, 3812–3815.

Wood, A. W., Chang, R. L., Levin, W., Thakker, D. R., Yagi, H., Sayor, J. M., Jerina, D. M., & Conney, A. H. (1984) *Cancer Res. 44*, 2320–2324.

Yagi, H., Thakker, D. R., Ittah, M., Croisy-Delcey, M., & Jerina, D. M. (1983) *Tetrahedron Lett. 24*, 1349–1352.

Zacharias, D. E., Kashino, S., Glusker, J. P., Harvey, R. G., Amin, S., & Hecht, S. S. (1984) *Carcinogenesis 5*, 1421–1430.